

Radical-Doped Metal–Organic Framework: Route to Nanoscale Defects and Magnetostructural Functionalities

Artem S. Poryvaev,^{†,§} Daniil M. Polyukhov,^{†,||} Eva Gjuzi,[‡] Frank Hoffmann,[‡] Michael Fröba,^{*,‡} and Matvey V. Fedin^{*,†,§}

[†]International Tomography Center SB RAS, Institutskaya str. 3a, Novosibirsk, 630090, Russia

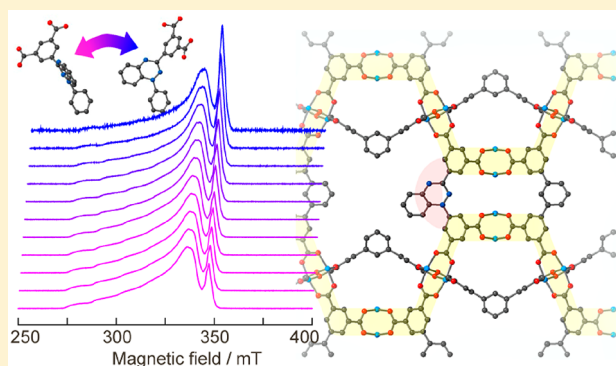
[‡]Institute of Inorganic and Applied Chemistry, University of Hamburg, Martin-Luther-King-Platz 6, 20146 Hamburg, Germany

[§]Novosibirsk State University, Pirogova str. 2, Novosibirsk, 630090, Russia

^{||}N.N. Vorozhtsov Institute of Organic Chemistry SB RAS, Novosibirsk, 630090, Russia

Supporting Information

ABSTRACT: Nanosized structural defects in metal–organic frameworks (MOFs) attract growing attention and often remarkably enhance functional properties of these materials for various applications. In this work, a series of MOFs [Cu₂(TPTA)_{1-x}(BDPBTR)_x] (H₄TPTA, [1,1':3',1''-terphenyl]-3,3'',5,5''-tetracarboxylic acid; H₄BDPBTR, 1,3-bis(3,5-dicarboxyphenyl)-1,2,4-benzotriazin-4-yl radical)) with a new stable radical linker doped into the structure has been synthesized and investigated using Electron Paramagnetic Resonance (EPR). Mixed linkers H₄TPTA and H₄BDPBTR were used to bridge copper(II) paddle-wheel units into a porous framework, where H₄BDPBTR is the close structural analogue of H₄TPTA. MOFs with various $x = 0–0.4$ were investigated. EPR studies indicated that the radical linker binds to the copper(II) units differently compared to diamagnetic linker, resulting in the formation of nanosized structural defects. Moreover, remarkable kinetic phenomena were observed upon cooling of this MOF, where slow structural rearrangements and concomitant changes of magnetic interactions were induced. Thus, our findings demonstrate that doping of structurally mimicking radical linkers into MOFs represents an efficient approach for designing target nanosized defects and introducing new magnetostructural functionalities for a variety of applications.



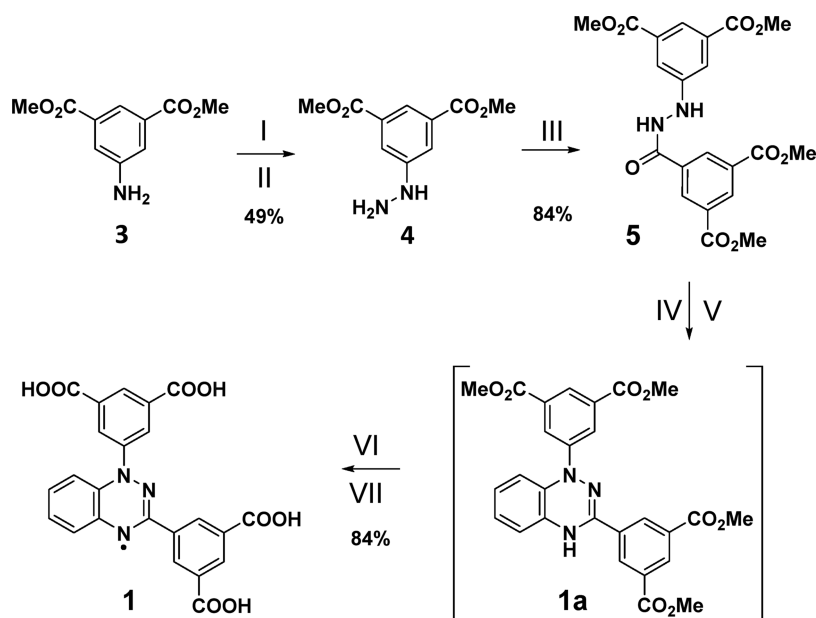
I. INTRODUCTION

Metal–organic frameworks (MOFs) are a fascinating class of self-assembling, porous crystalline materials, which are built up by the coordination of metal ions or clusters with organic bridging ligands.^{1–3} Since their discovery over 20 years ago, the field of MOFs has been marked by astonishing development and enormous interest of the scientific community and industry. Such high appeal is due to the MOFs high structural and functional adjustability that makes them amenable for an ever-expanding potential for application scope.^{4–7} In addition to applications such as gas storage and separation,^{8–11} catalysis,^{12,13} chemical sensor technology,¹⁴ and drug release,¹⁵ which have been investigated for some time, MOFs with special properties like magnetism,¹⁶ luminescence,¹⁷ ferroelectricity,¹⁸ redox activity,¹⁹ switchable behavior,²⁰ and proton conductivity²¹ are attracting increasing interest today. Remarkably, in a number of contexts it was found that nanosized structural defects occurring in MOFs might strongly enhance their functionalities in gas uptake, catalysis, and many other various applications.^{22–24}

Magnetic properties in MOFs usually are introduced by open-shell metal ions or lanthanide ions.^{16–18} The famous MOF Cu₃(btc)₂, also known as HKUST-1, shows relatively strong antiferromagnetic coupling as this MOF is built up by dimeric copper(II) paddle-wheel (PW) units. However, there is only a very weak exchange between neighboring PWs.²⁵ The reason is that the size of even short diamagnetic linker bridges prevents spin coupling throughout the framework, meaning that the dimeric units remain magnetically isolated. A potential way of designing MOFs with long-range magnetic order, therefore, is to introduce spin density between the metal centers. The growing family of stable organo radicals is a suitable choice in this case.²⁶

Radicals can be incorporated into MOFs in different ways: by way of noncovalently bound guests within the voids, as pendant radicals on metals or ligands,^{27,28} and in the form of structurally integrated organic radicals.^{29,30} However, the only way to obtain long-range magnetic ordering is to use

Received: March 11, 2019

Scheme 1. Synthesis of Radical Linker H₄BDPBTR 1^a

^aReagents and conditions: (I) NaNO₂, HCl (37%), EtOH, H₂O, 2 h, -1 °C; (II) SnCl₂·2H₂O, HCl (37%), 2 h, rt; (III) dimethyl 5-(chlorocarbonyl)benzene-1,3-dioate, THF, NEt₃, 4.5 h, 0 °C - rt; (IV) *o*-iodoaniline, CuI, K₂CO₃, DMSO, Ar, 15 h, 90 °C; (V) AcOH, 10 min, 140 °C; (VI) NaOH (aq, 2 M), DCM, 18 h, rt; (VII) KOH, H₂O, THF, 3 h, reflux, HCl (1 M).

structurally integrated radical linkers as rigid spin mediators between the inorganic building units.³¹ A well-suited radical linker candidate for realizing such MOFs is based on the benzotriazin-4-yl motif, also known as Blatter's radical. Due to the extended conjugated π -system this radical has a high thermal and chemical stability, even in air.^{32,33} The additional benefits of this radical are the structural adaptability and the already proven application for metal coordination.^{34–37}

In this work we report the synthesis and investigation of the new MOF series Cu₂(TPTA)_{1-x}(BDPBTR)_x (H₄TPTA, [1,1':3',1''-terphenyl]-3,3'',5,5''-tetracarboxylic acid 2; H₄BDPBTR, 1,3-bis(3,5-dicarboxyphenyl)-1,2,4-benzotriazin-4-yl radical) 1) with a novel stable radical linker integrated in different concentrations into a framework resembling the PCN-306 host structure.³⁸ Since both radicals and copper(II) ions are paramagnetic, we employ methods of Electron Paramagnetic Resonance (EPR) for characterization of structural and magnetic properties of these MOFs. EPR methods proved to be very useful in studies of structure and functions of MOFs recently.^{39–56} Pulse and continuous wave (CW) EPR techniques were also actively used to study MOFs containing copper(II) PW units,^{48–56} but hitherto not for MOFs containing additionally radical organic linkers. Below we describe our variable-temperature CW and pulse EPR studies of Cu₂(TPTA)_{1-x}(BDPBTR)_x aiming at deriving key structural information on the coordination modes of the radicals and generated structural defects, the spin-coupling behavior between radicals and the PW units, and the flexibility of the frameworks of this type.

II. EXPERIMENTAL SECTION

II.1. General Methods and Materials. All solvents were used in HPLC grade quality. All reagents and solvents were purchased from commercial sources and used as received without further purification. Dimethyl 5-(chlorocarbonyl)benzene-1,3-dioate was prepared according to literature procedures.⁵⁷

MOFs were activated in vacuum at room temperature after the following solvent exchange protocol was performed under an argon atmosphere. The synthesis solvent was exchanged against tetrahydrofuran three times, followed by an exchange against dichloromethane once. The solvent was replaced with fresh solvent after each 24 h.

Powder X-ray diffraction (PXRD) measurements were carried out at room temperature using a Panalytical MPD X'Pert Pro X-ray diffractometer with Cu/K α radiation. The standard angle range was $2\theta = 5\text{--}50^\circ$, with a step width of 0.1° and a counting time of 20 s. The evaluation was done with the software X'Pert HighScore Plus 2.2.5 from PANalytical.

Nitrogen physisorption measurements were recorded with a Quantachrome QUADRASORB-SI-MP at 77 K. The specific surface area was determined by using the Brunauer–Emmett–Teller (BET) micropore assistant provided in the Quantachrome ASiQwin software.

EPR studies were performed using commercial Bruker Elexsys E580 X/Q-band EPR spectrometer equipped with Oxford Instruments temperature control system ($T = 4\text{--}300$ K). In all cases, powdered samples were placed into the quartz sample tubes (OD = 2.8 mm) and sealed off at vacuum. CW EPR spectra were recorded at conditions avoiding unwanted modulation broadening. Two-pulse Hahn echo sequence $\pi/2\text{--}\tau\text{--}\pi\text{--}\tau\text{--}\text{echo}$ was used to record echo-detected EPR spectra, and a standard HYSORE (Hyperfine Sublevel Correlation Spectroscopy) sequence was used for nuclear modulation experiments (pulse lengths 12/24 ns for $\pi/2$ and π flip angles).⁵⁸ For all simulations EasySpin toolbox for Matlab was used.⁵⁹

II.2. Synthesis. Synthesis of the Diamagnetic Linker H₄TPTA. Synthesis of [1,1':3',1''-terphenyl]-3,3'',5,5''-tetracarboxylic acid (2, H₄TPTA) was carried out according to Liu et al.³⁸

Synthesis of the Radical Linker H₄BDPBTR 1. Following Scheme 1, dimethyl 2-aminobenzene-1,3-dicarboxylate 3 was converted to the hydrazine 4 via the diazonium salt. Hydrazide 5 was obtained by addition of dimethyl 5-(chlorocarbonyl)benzene-1,3-dioate under hydrogen chloride cleavage. Based on a synthesis of the group of Koutentis, a one-pot-like synthesis without purification of the intermediates was performed to provide the radical linker 1.⁶⁰ The synthesis can be classified by four steps: the copper-catalyzed Ma cross-coupling between hydrazide 5 and *o*-iodoaniline, a cyclization step in boiling glacial acetic acid, the oxidation of the triazine 1a in the

presence of base, and completion of methyl ester cleavage, followed by precipitation of the linker **1** under mild acidic conditions (see Section I of Supporting Information (SI) for characterization).⁶¹

Synthesis of the Mixed-Linker Radical-Containing MOFs. In a typical synthesis of $\text{Cu}_2(\text{TPTA})_{1-x}(\text{BDPBTR})_x$, a solution of the respective linkers and copper(II) nitrate trihydrate in *N,N*-dimethylformamide (DMF) was acidified with nitric acid and the reaction mixture was treated solvothermally for 7 d at 60 °C under an argon atmosphere in a crimped glass. This procedure furnished blue to black (depending on x , i.e., the ratio of the radical to nonradical linker composition) nanocrystalline powder.

III. RESULTS AND DISCUSSION

III.1. Structural Characterization. A series of compounds $[\text{Cu}_2(\text{TPTA})_{1-x}(\text{BDPBTR})_x]$ with different amount of radical linker $x = 0-0.4$ (for brevity, below we use designations “ $x = \dots$ MOF”) were synthesized and characterized using PXRD and nitrogen physisorption. The integrity of the reisolated linkers was investigated by ^1H NMR spectroscopy (Figure S13). Unfortunately, the radical linker was found to be not stable enough in the presence of copper salts, meaning that the actual content of radical linkers that is incorporated into the MOF is lower compared to the content in the initial synthesis mixture (see SI and the next section). More important, the crystallinity of the MOF decreases progressively upon addition of radical linker (Figure 1b). When more than 40% of radical linker is introduced ($x > 0.4$), only an amorphous phase can be detected. Results from nitrogen physisorption correlate with this finding (Figure 1c). For initial linker amounts higher than

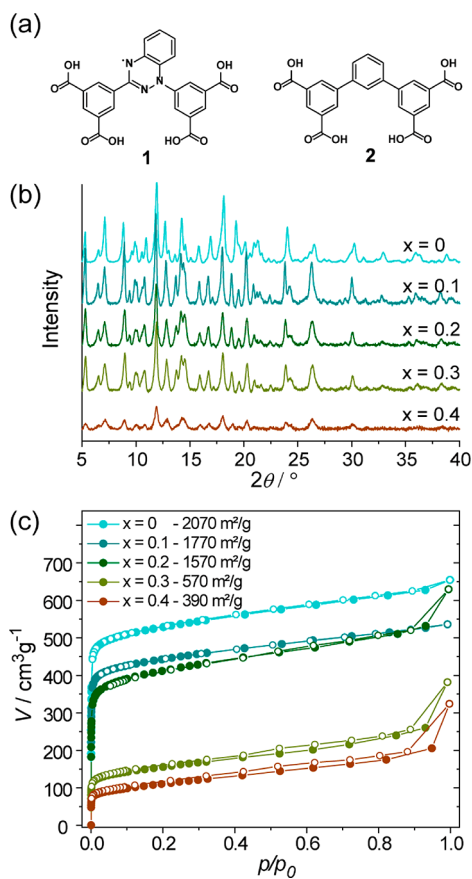


Figure 1. Chemical structure of the building blocks of studied MOFs (a), PXRD data for $x = 0-0.4$ (b), and nitrogen physisorption isotherms of activated MOFs measured at 77 K, $x = 0-0.4$ (c).

20%, the obtained surface area decreases significantly. Since single-crystal study was not available for this series of MOFs, we implemented EPR for obtaining the complementary structural information and elucidation of magnetic interactions.

III.2. Paramagnetic Sites and Magnetic Motif. In principle, there can be two types of paramagnetic centers in such radical-containing MOFs: dimeric copper(II) sites in the PW units and radical centers. In addition, previous studies of the PW containing MOFs have indicated that often signals of single copper(II) can be present as well.⁴⁸ These can be either copper(II) sites in defect PWs where, for some reason, the second copper ion is in diamagnetic copper(I) oxidation state. Alternatively, there can be some extra-framework monomeric copper(II) species located inside the pores of MOFs and giving characteristic EPR signals.⁴⁸

Figure 2 shows the variable-temperature CW EPR data for $x = 0.1$ MOF (see Figures S19 and S20 in SI for $x = 0$ and 0.2 MOFs).

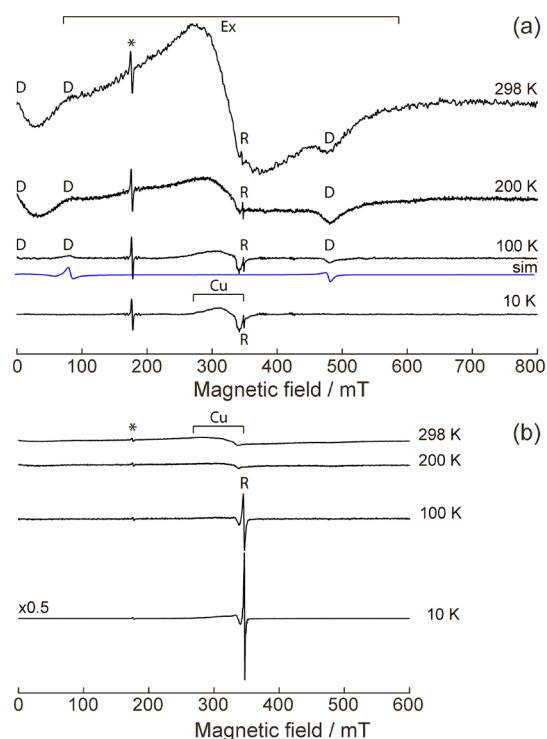


Figure 2. X-band CW EPR spectra of $x = 0.1$ MOF vs temperature (indicated on the right). Signal of single copper(II) is marked by “Cu”, of free radical by “R”, of dimeric copper(II) paddle-wheel units by “D”, of exchange-narrowed line as “Ex”, of internal reference in the resonator by asterisk. (a) High mw power I_1 . The spectra at 100–298 K are normalized to the internal reference. Blue trace shows the simulation of spectrum at $T = 100$ K. (b) Low mw power $I_2 = I_1/1000$. The spectra are normalized to the internal reference, the spectrum at $T = 10$ K is scaled by a factor of 0.5.

Different species in this sample have much different electron relaxation times. In order to observe fast-relaxing copper(II) dimers we need to apply high microwave (mw) power, which leads to a suppression of signal of slow-relaxing radical due to a mw saturation. Therefore, Figure 2a,b shows the EPR spectra recorded at two values of mw power differing by a factor of 1000 (30 db).

At both values of mw power, depending on temperature, we observe signals of copper(II) dimers in the PWs (D), signals of

radicals (R), signals of single copper(II) (Cu), and broad exchange-narrowed line (Ex). It is well-known for the PWs that the exchange coupling between two copper(II) ions is strong and antiferromagnetic (singlet–triplet splitting $\sim 220\text{ cm}^{-1}$); therefore, at temperatures below $\sim 80\text{ K}$ all dimeric copper(II) units become EPR-silent.^{48,62} As the temperature increases, the excited triplet state becomes populated, giving rise to the dimeric signals, most clearly visible at 100 and 200 K. Simulation yields zero-field splitting (ZFS) parameters typical for the copper(II) PWs: $D = 328\text{ mT}$ (0.306 cm^{-1}) and $E \approx 0$.^{48,62} Upon further population of the triplet state, the probability of finding neighboring copper(II) PWs in paramagnetic state becomes high enough and the spectrum begins to coalesce (the phenomenon known as exchange narrowing⁶³). The spectrum at 298 K is clearly contributed by a broad exchange-narrowed line on top of the smoothed dimeric signals, meaning that the exchange coupling between neighboring PWs becomes significant. Note that the spectral changes with temperature shown in Figure 2 and Figure S19 (SI) are very similar to those reported previously for variable-temperature CW EPR on copper(II) PW containing MOF $\text{Cu}_3(\text{btc})_2(\text{H}_2\text{O})_3$ (without any radical linkers).⁴⁸ Therefore, based on the analysis of variable temperature CW EPR, we propose that exchange interaction pathways propagate between PWs via the connecting phenyl rings (Figure 3).

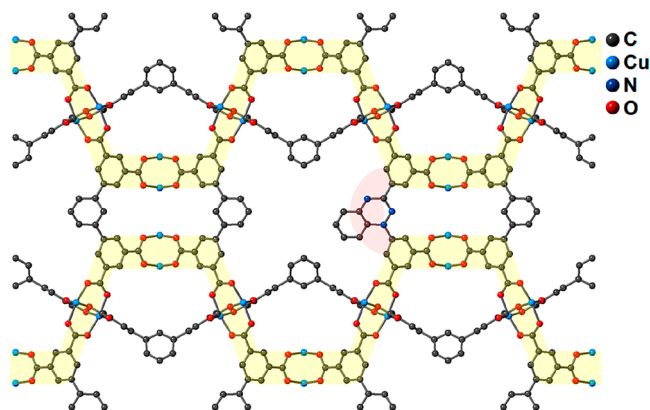


Figure 3. Exchange interaction pathways in $x = 0$ and 0.1 MOFs (anticipated structure) at high temperature limit. The pathways inherent for $x = 0$ MOF are shaded in yellow, the additional pathway via the radical linker in $x = 0.1$ MOF is shaded in red.

At $T = 10\text{ K}$ all copper(II) PWs are in the ground $S = 0$ state, and we observe only signals of single copper(II) and organic radical (Figure 2b). However, as the temperature increases, the signal of organic radical ($g \sim 2.0$) decreases and disappears completely at $T = 200\text{ K}$ and above (Figure 2b). This unambiguously means that the radical becomes involved in the exchange-coupled network of the PWs at high temperatures and conducts electron density between parallel magnetic chains (Figure 3).

The signals of the single copper(II) (Cu) are observed at 10 K for any value of x (Figures 2 and S21). The analysis of temperature-dependent CW EPR data allows us to estimate the ratio of single to dimeric copper(II) sites (Figures 2, S19, and S20), which gives approximately 1, 3, and 20% of single copper(II) for $x = 0, 0.1,$ and $0.2,$ respectively. The increase of the single copper(II) contribution at higher x can also be clearly seen in Figure S21 (SI).

Using the obtained concentrations of single copper(II), we can also obtain the concentration of radicals on the basis of EPR spectra at 10 K (Figure 2b). The calculated concentration of radicals in $x = 0.1$ MOF does not exceed $\sim 2\%$ relative to the overall amount of linkers (instead of expected 10%). This unambiguously means that the radicals partly decompose or are coupled with other paramagnetic sites in the MOF. Since an increase in the amount of loaded radical linkers correlates with a larger amount of single copper(II) sites, we plausibly conclude that the radicals either perturb the formation of copper(II) PW units, or they couple with one of the copper(II) sites in the formed PWs resulting in EPR-silent copper-radical dyads. In the latter case, the second (uncoupled) copper(II) ion in the PW becomes EPR-visible. The absolute numbers for the concentration of single copper(II) and the amount of loaded radical linker agree only qualitatively (10% loading yields $\sim 3\%$ of single copper(II), 20% loading yields $\sim 20\%$ of single copper(II)). The reason for poor quantitative agreement is, perhaps, the uncontrolled amount of extra-framework copper(II) species, which can also form diamagnetic complexes with radical linker either during the synthesis or postsynthetically.

In order to study the local coordination environment of single copper(II) centers, we applied pulse EPR method HYSCORE (Hyperfine Sublevel Correlation Spectroscopy),⁶⁴ which allows revealing the weak hyperfine interactions (HFIs) between electron spin of copper(II) and neighboring nuclear spins. Figure 4 shows the HYSCORE spectra obtained on the single copper(II) signals for MOFs with $x = 0$ and 0.1 at two magnetic field positions $B = 285\text{ mT}$ (g_{\parallel} orientation) and $B = 338\text{ mT}$ (g_{\perp} region). First, the signals due to the HFIs with surrounding protons are visible near their Larmor frequency $\nu(^1\text{H}) \sim 14\text{ MHz}$. These proton spectra are drastically different in the two orientations: the couplings observed at g_{\parallel} orientation (Figure 4a, wide ridges across diagonal) are much larger compared to those at g_{\perp} orientation (Figure 4b). This implies the presence of close proton(s) in axial coordination of copper(II), whereas in equatorial plane mainly remote protons are visible. Simulation of HYSCORE spectra at g_{\parallel} orientation (Figure S25) shows that the dipolar HFI is $T \approx 1.7\text{ MHz}$, which translates into electron–nucleus distance of $\sim 3.6\text{ \AA}$. Therefore, the obtained data can be most plausibly rationalized by assuming that single copper(II) centers are localized in the PW units with an additional axial ligand being the DMF molecule, whose aldehyde proton is $3.6\text{--}4\text{ \AA}$ away from the copper(II). The abundance of DMF molecules unremovable from MOF by our activation protocol was also supported by CHN analysis (Table S2, SI), whereas the octahedral geometry of the copper(II) environment is confirmed by the analysis of its echo-detected EPR spectrum (Figure S26).

More importantly, in the case of $x = 0.1$ MOF we observe strong enhancement of signals with $\nu \sim 1\text{ MHz}$ compared to $x = 0$ MOF. These signals are clearly enhanced in both field positions, and can only be assigned to the nitrogen (^{14}N) nuclei emerged around the single copper(II) spins (Figure S25). Given that actual amounts of radical and single copper(II) in $x = 0.1$ MOF are $\sim 2\%$ and $\sim 3\%$, respectively, it is statistically improbable that the single copper(II) spontaneously locates near the radical linker. Therefore, HYSCORE data prove that the formation of the single copper(II) is driven by the radical linker, resulting in their close mutual location. In other words, the radical linker

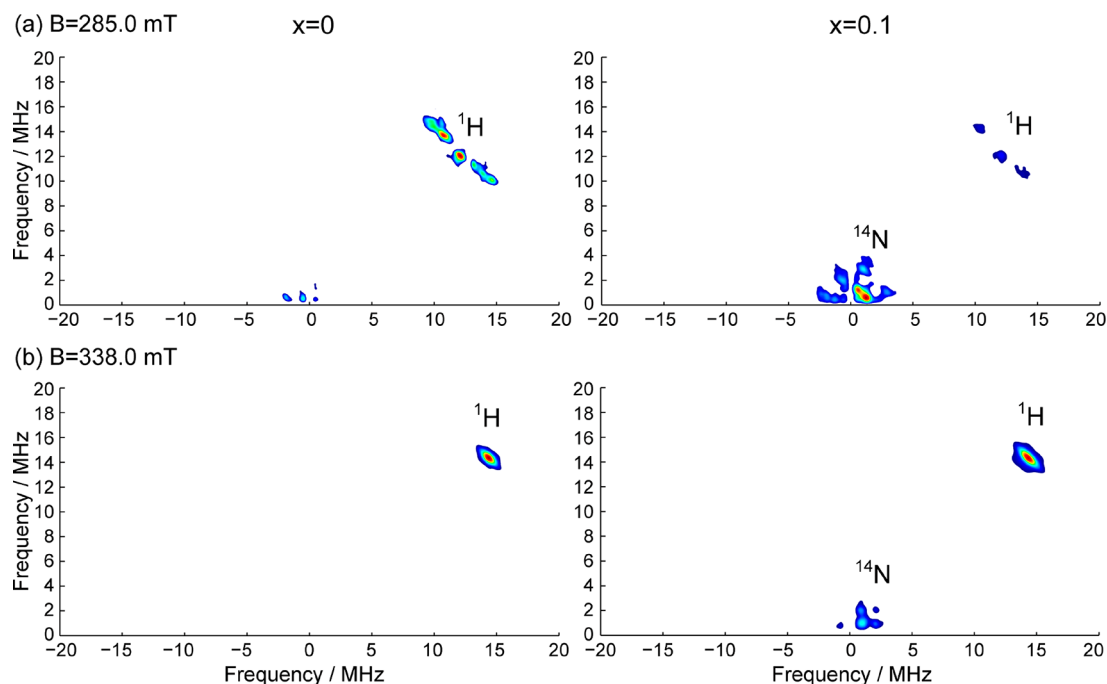


Figure 4. X-band HYSCORE spectra of MOFs with $x = 0$ (left) and 0.1 (right) detected at two field positions 285 (a) and 338 mT (b). The regions of ^1H and ^{14}N signals (for $x = 0.1$) are marked.

perturbs the local MOF structure and causes single copper(II) defect sites.

Finally, variable-temperature CW EPR data on $x = 0.2$ compound shed further light into formation of single copper(II) defects and the role of radical linker (Figure S20). Remarkably, no characteristic signals of dimers are visible at any temperatures for this sample, nor the broad line of extended exchange-coupled network of the PW units. This likely means that already for $x = 0.2$ there is a strongly decreased amount of PW units where both copper(II) ions are paramagnetic. As is evident from Figure 1 above, the material becomes more amorphous upon increase of the radical content x , and at the same time the number of paramagnetic copper(II)–copper(II) dimers decreases.

In summary, EPR studies indicate that the radical linkers bind to the copper(II) units differently compared to diamagnetic linkers and introduce structural defects in their vicinity. This is in perfect agreement with the trend of decreasing crystallinity upon increasing x , as revealed by PXRD. The doping of radical linkers leads to a formation of single copper(II) defects in the PWs, meaning that the second copper is reduced to the diamagnetic copper(I) state. Below we expand on this idea and propose that the radical linker is the “dangling linker” type of defect in MOF, which is attached by two carboxylate groups to the PW on the one side, but freely dangles on the other. We also propose possible scenario why such mismatch leads to a formation of mixed-valence defect PWs.

III.3. Temperature-Induced Slow Structural Rearrangements. Pulse EPR experiments discussed in the previous section were recorded at liquid helium temperatures about 10 K. At such temperatures CW EPR studies on radical and single copper(II) sites are problematic due to severe microwave saturation, but pulse EPR becomes straightforward to implement. Surprisingly, in addition to the results discussed above, these studies revealed some peculiar kinetic phenomena

occurring in such MOFs. We noticed that when a sample is placed at 10 K, its echo-detected (ED) EPR spectrum evolves on the time scale of several hours (Figure 5). Thermalization of the sample in the cryostat of our spectrometer normally takes a few minutes, and after a maximum of 15–20 min the sample reaches perfect equilibrium with the cryostat. This was specially verified once again under the same conditions using several reference samples, and in all cases complete thermalization was achieved within half an hour. It could also be

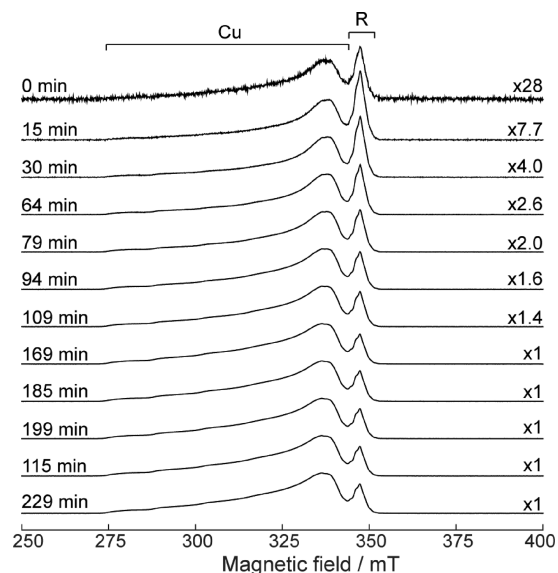


Figure 5. Pulse (echo-detected) EPR spectra of $x = 0.1$ MOF, taken from room temperature, then inserted into 10 K and measured as a function of time. Time delay after insertion is shown on the left, magnification factor is shown on the right. Signal assignment is sketched on top, where “Cu” refers to the single copper(II) defects and “R” to the radical.

hypothesized that thermal contact/conductivity of highly porous material sealed off at vacuum in the quartz tube is much lower compared to common samples. To verify this, we used another reference MOF sample⁴⁵ containing copper(II) PWs: Cu-doped $[\text{Zn}_2(1,4\text{-bdc})_2(\text{dabco})]$ prepared for EPR measurement in the same way, whose physical properties must not be noticeably different. Figure 6 shows that there is no further signal growth beyond ~ 30 min after insertion of the sample into the cryostat.

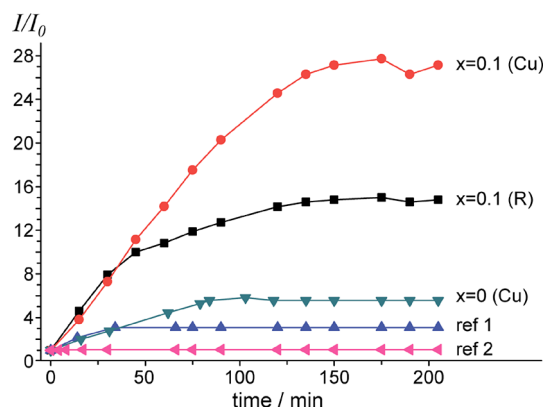


Figure 6. Intensities of pulse EPR signals measured as a function of time upon insertion of sample into 10 K. Intensities of single copper defects (Cu) and free radical (R) signals in $x = 0.1$ MOF are plotted, the intensity of Cu in $x = 0$ MOF, and, finally, the intensity of copper(II) signal in reference MOF Cu(II)-doped $[\text{Zn}_2(1,4\text{-bdc})_2(\text{dabco})]$, bare (ref 1) and loaded with CO_2 (ref 2). Y-axis shows the normalized echo intensity (I_0 is the intensity immediately after insertion of sample into cryostat).

In the case of $x = 0.1$ MOF shown in Figure 5, we observed the growth of both signals of single copper(II) and radical versus time after insertion at 10 K. The overall increase of intensity is dramatic, being about 30-fold during 4 h (Figure 6). Very similar behavior was observed for $x = 0.05$ MOF (Figure S23). In the case of $x = 0$, we detected much weaker growth (~ 6 -fold) completed within shorter time (~ 75 min). In the case of $x = 0.2$, no kinetic effects were observed, perhaps due to the high amount of defect sites and relatively low crystallinity of the structure. Thus, we conclude that kinetic effects are moderately present in $x = 0$ radical-free MOF, they are noticeably enhanced for $x = 0.05\text{--}0.1$, and they disappear for $x = 0.2$ and higher. This is all coherent with the previous conclusions that doping of radical linkers introduces structural defects in this MOF, still keeping its crystallinity bearable at small x , but ultimately losing it at $x > 0.4$.

Slow kinetic effects must be connected to some structural rearrangements (see below), and, generally, many flexible MOFs exhibiting guest- or temperature-induced rearrangements are known.^{65–69} We speculate that incorporation of small amounts of defects for $x = 0.05\text{--}0.1$ MOFs makes the local structure more fragile and prone to rearrangements. It is overall unlikely that the whole structure of MOF undergoes rearrangement; however, local structure of the defect sites might be more flexible and have more freedom for conformational change without perturbing much the regular lattice.

Then why are these rearrangements so slow? In principle, it is known that some bistable compounds can be kinetically trapped in a high-temperature structural state upon shock-freezing. For example, in spin-crossover research such an effect

is known as Temperature-Induced Excited Spin State Trapping (TIESST).^{70,71} We therefore suppose that the origin of the observed phenomena in our MOFs can be generally similar.

For most of the materials, the thermal capacity drastically drops down with temperature. This means that, given the same temperature gradient, the cooling rate accelerates at low T . Having this in mind, we compared the kinetic effects for $x = 0.1$ MOF in two situations: (i) the sample was kept for ~ 4 h at room temperature and then introduced into cryostat at 10 K (the experiments discussed above), and (ii) the sample was thermalized in liquid nitrogen ($T = 77$ K) for ~ 4 h and then immediately introduced into cryostat at 10 K. The kinetic behavior in both cases is illustrated in Figure S27 (SI). No remarkable differences were found between (i) and (ii), except for some minor changes in the shapes of kinetic curves at short times. This means that the structural trapping occurs essentially during the temperature change below $T < 77$ K. This also once again confirms that the observed kinetic phenomena do not owe to the slow thermalization of the sample, because in this case, one would reasonably assume that the temperature jump from 293 to 10 K would require more time than the jump from 77 to 10 K.

Finally, we investigated the electron relaxation rate of single copper(II) and radical centers vs time after the sample was placed to 10 K (Figure S24). If relaxation rates of copper(II) and radical would change with time differently, this could impact their relative intensities in ED EPR spectra and be one more explanation of the observed kinetic phenomena. However, no noticeable changes in longitudinal relaxation (T_1) were observed versus time, proving that the evolution of the spectral shapes in Figure 5 owes purely to the changing amounts of copper(II) and radical centers.

The data in Figures 5 and 6 clearly indicate that the amount of spins visible by pulse EPR grows with time, and this is also confirmed qualitatively by CW EPR (Figure S22). Remarkably, the overall growth of the signal of single copper(II) defects is two times larger than that of the radical, for both $x = 0.1$ and 0.05 samples. This means, that kinetic process leads to the “formation” of two EPR-visible single copper(II) ions per one EPR-visible radical. This might happen if the fragile high-temperature (HT) structure incorporates exchange-coupled (not covalently bound) spin triads, where signals of closely located copper(II) defects and/or radical centers are strongly broadened and therefore EPR-invisible. The low-temperature (LT) structure should have these paramagnetic centers better separated from each other, resulting in the onset of their individual EPR signals.

At the moment we cannot provide the exact structural model for such rearrangement; however, we can propose a plausible scenario for that. The radical linker has slightly different geometry compared to the diamagnetic analogue. Therefore, it likely binds to the PW via carboxylate groups on the one end with high efficiency, but the binding on the other end can be hindered, leading to a “dangling linker” defect in the MOF structure (Figure 7). In this case, the two neighboring PWs should have vacant copper(II) sites becoming accessible for competing reactions. In our preparation conditions (thermal treatment) DMF easily decomposes to formaldehyde, which is able to reduce copper(II) to copper(I) and produce formate that readily occupies vacant positions in the PWs. Very recently, Fu et al. carried out Density Functional Theory (DFT) calculations on defective Zr clusters that are present in UiO-66 and found out that “missing linker” Zr defective sites

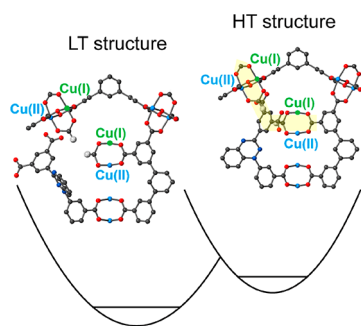


Figure 7. Sketch of the two potential wells corresponding to the two hypothetical structures, which refer to the high-temperature (HT) and low-temperature (LT) conformations of the dangling BDPBTR linker. Low temperature structure corresponds to spatially separated copper(II) and radical centers, whereas high-temperature (kinetically trapped) structure has closely located copper(II) and radical ions and stronger exchange coupling between them (shaded in yellow).

can be considerably stabilized by bridging bidentate binding acetate species or also by a mixture of acetate and water, each in monodentate binding mode.⁷² In such case, we arrive at the dangling radical linker and two mixed-valence copper(II)–copper(I) units next to it (Figure 7). In order to explain the kinetic phenomena, we need to assume that the dangling linker has two preferred orientations with the outer phenyl ring being closer to or farther away from the mixed-valence PW (high- and low-temperature structures, respectively). The two orientations (two potential minima in Figure 7) can possibly originate from two conformations of the linker (folded or twisted). Alternatively, they can be the consequence of a subtle thermal shrinking/expansion of the MOF itself. Note that similar explanation can also be applied to the less pronounced (but still present) kinetic phenomena in $x = 0$ MOF (Figure 6), with the only difference that radical center is not involved.

Last but not least, we have found that the ability of kinetic behavior depends on the sample aging. Freshly prepared samples do show kinetic effects, but after keeping the samples in an argon atmosphere for 3–6 months the above effects get noticeably smaller and fully disappear in approximately 1 year.

CONCLUSIONS

In this work, the free radical bearing mixed-linker MOF series $[\text{Cu}_2(\text{TPTA})_{1-x}(\text{BDPBTR})_x]$ was synthesized and characterized with PXRD, nitrogen physisorption and extensively studied by EPR. The progressive decrease of the crystallinity upon increase of x was evidenced by PXRD, and above $x \sim 0.4$, the material appears to be fully amorphous. Physisorption measurements correlate with this result and are presenting a loss of porosity already above $x \sim 0.2$. In agreement with this, CW and pulse EPR indicate that the radical linker H_4BDPBTR reacts with the copper precursor complex differently compared to diamagnetic linker H_4TPTA . In particular, the amount of single copper(II) centers increases upon addition of radical linker in a series of $x = 0, 0.1$, and 0.2 , implying the increasing amount of nanosized defects in the structure. At the same time, HYSCORE indicates the presence of ^{14}N nuclei coming from H_4BDPBTR linker surrounding single (defect) copper(II) sites for $x = 0.1$. Thus, doping radical linker of generally close structure into $\text{Cu}_2(\text{TPTA})$ MOF results in generation of point defects in the framework, and for a small concentrations of radical linker (e.g., 5–10%) the initial structure, crystallinity, and porosity of the host MOF remain unperturbed.

Surprisingly, for $x = 0.05–0.1$, the defected structure reveals noticeable slow structural rearrangements upon shock-freezing at liquid helium temperatures. The local high-temperature structure of the defect sites appears to be kinetically trapped and relaxes to a low-temperature structure on a time scale of a few hours. Upon such structural rearrangement, which can be reversed by heating, the magnetic interactions and properties of the MOF are modulated.

A number of works addressed the role of the nanosized structural defects in MOFs recently. Such defects, either inherent or deliberately engineered, might remarkably enhance functional properties of these materials for applications as gas separation and storage, catalysis and, potentially, many more.^{22–46} Our present work clearly underlines that introduction of structurally mimicking radical linkers into MOFs is an interesting and promising approach for generation of site defects and bringing new magnetostructural functionalities into MOFs. This strategy is to be explored in more detail and applied in MOF research in the future.

ASSOCIATED CONTENT

Supporting Information

The Supporting Information is available free of charge on the ACS Publications website at DOI: 10.1021/acs.inorgchem.9b00696.

Supplementary characterization data of the synthesized linkers (procedure, IR, NMR, TG/MS, elemental analysis) and supplementary EPR data (PDF)

AUTHOR INFORMATION

Corresponding Authors

*E-mail: froeba@chemie.uni-hamburg.de.

*E-mail: mfedin@tomo.nsc.ru.

ORCID

Matvey V. Fedin: 0000-0002-0537-5755

Notes

The authors declare no competing financial interest.

ACKNOWLEDGMENTS

This work was supported by RFBR (18-29-04013). We are very thankful to P. A. Demakov and Prof. Dr. D. N. Dybtsev (NIIC SB RAS) for providing us with the reference sample $\text{Cu}(\text{II})$ -doped $[\text{Zn}_2(1,4\text{-bdc})_2(\text{dabco})]$. D.M.P. thanks the Ministry of Science and Higher Education (MSHE) of the Russian Federation (Grant 14.W03.31.0034). We thank MSHE for access to the EPR equipment.

REFERENCES

- (1) Yaghi, O. M.; Li, G.; Li, H. Selective Binding and Removal of Guests in a Microporous Metal-Organic Framework. *Nature* **1995**, *378*, 703–706.
- (2) Li, H.; Eddaoudi, M.; O’Keeffe, M.; Yaghi, O. M. Design and Synthesis of an Exceptionally Stable and Highly Porous Metal-Organic Framework. *Nature* **1999**, *402*, 276–279.
- (3) Férey, G. Hybrid Porous Solids: Past, Present, Future. *Chem. Soc. Rev.* **2008**, *37*, 191–214.
- (4) Stock, N.; Biswas, S. Synthesis of Metal-Organic Frameworks (MOFs): Routes to Various MOF Topologies, Morphologies, and Composites. *Chem. Rev.* **2012**, *112*, 933–969.
- (5) Kirchon, A.; Feng, L.; Drake, H. F.; Joseph, E. A.; Zhou, H.-C. From Fundamentals to Applications: a Toolbox for Robust and Multifunctional MOF Materials. *Chem. Soc. Rev.* **2018**, *47*, 8611–8638.

- (6) Yuan, S.; Feng, L.; Wang, K.; Pang, J.; Bosch, M.; Lollar, C.; Sun, Y.; Qin, J.; Yang, X.; Zhang, P.; Wang, Q.; Zou, L.; Zhang, Y.; Zhang, L.; Fang, Y.; Li, J.; Zhou, H.-C. Stable Metal-Organic Frameworks: Design, Synthesis, and Applications. *Adv. Mater.* **2018**, *30*, 1704303.
- (7) Doherty, C. M.; Buso, D.; Hill, A. J.; Furukawa, S.; Kitagawa, S.; Falcaro, P. Using Functional Nano- and Microparticles for the Preparation of Metal-Organic Framework Composites with Novel Properties. *Acc. Chem. Res.* **2014**, *47*, 396–405.
- (8) Han, X.; Godfrey, H. G. W.; Briggs, L.; Davies, A. J.; Cheng, Y. Q.; Daemen, L. L.; Sheveleva, A. M.; Tuna, F.; McInnes, E. J. L.; Sun, J. L.; Drathen, C.; George, M. W.; Ramirez-Cuesta, A. J.; Thomas, K. M.; Yang, S. H.; Schroder, M. Reversible Adsorption of Nitrogen Dioxide within a Robust Porous Metal-Organic Framework. *Nat. Mater.* **2018**, *17*, 691–696.
- (9) Knebel, A.; Geppert, B.; Volgmann, K.; Kolokolov, D. I.; Stepanov, A. G.; Twiefel, J.; Heitjans, P.; Volkmer, D.; Caro, J. Defibrillation of Soft Porous Metal-Organic Frameworks with Electric Fields. *Science* **2017**, *358*, 347–351.
- (10) Li, J. R.; Kuppler, R. J.; Zhou, H. C. Selective Gas Adsorption and Separation in Metal-Organic Frameworks. *Chem. Soc. Rev.* **2009**, *38*, 1477–1504.
- (11) Li, H.; Wang, K.; Sun, Y.; Lollar, C. T.; Li, J.; Zhou, H.-C. Recent Advances in Gas Storage and Separation Using Metal-Organic Frameworks. *Mater. Today* **2018**, *21*, 108–121.
- (12) Gascon, J.; Corma, A.; Kapteijn, F.; Xamena, F. X. L. I. Metal Organic Framework Catalysis: Quo vadis? *ACS Catal.* **2014**, *4*, 361–378.
- (13) Sartor, M.; Stein, T.; Hoffmann, F.; Fröba, M. A New Set of Isorecticular, Homochiral Metal-Organic Frameworks with upc Topology. *Chem. Mater.* **2016**, *28*, 519–528.
- (14) Robinson, A. L.; Stavila, V.; Zeitler, T. R.; White, M. I.; Thornberg, S. M.; Greathouse, J. A.; Allendorf, M. D. Ultrasensitive Humidity Detection Using Metal-Organic Framework-Coated Microsensors. *Anal. Chem.* **2012**, *84*, 7043–7051.
- (15) Peikert, K.; McCormick, L. J.; Cattaneo, D.; Duncan, M. J.; Hoffmann, F.; Khan, A. H.; Bertmer, M.; Morris, R. E.; Fröba, M. Amino substituted $\text{Cu}_3(\text{btc})_2$: a New Metal-Organic Framework with a Versatile Functionality. *Microporous Mesoporous Mater.* **2015**, *216*, 118–126.
- (16) Dong, R.; Zhang, Z.; Tranca, D. C.; Zhou, S.; Wang, M.; Adler, P.; Liao, Z.; Liu, F.; Sun, Y.; Shi, W.; Zhang, S.; Zschech, E.; Mannsfeld, S. C. B.; Felsler, C.; Feng, X. A Coronene-Based Semiconducting Two-Dimensional Metal-Organic Framework with Ferrimagnetic Behavior. *Nat. Commun.* **2018**, *9* (1), 1–9.
- (17) Bauer, C. A.; Jones, S. C.; Kinnibrugh, T. L.; Tongwa, P.; Farrell, R. A.; Vakil, A.; Timofeeva, T. V.; Khrustalev, V. N.; Allendorf, M. D. Homo- and Heterometallic Luminescent 2-D Stilbene Metal-Organic Frameworks. *Dalton Trans.* **2014**, *43*, 2925–2935.
- (18) Darago, L. E.; Aubrey, M. L.; Yu, C. J.; Gonzalez, M. I.; Long, J. R. Electronic Conductivity, Ferrimagnetic Ordering, and Reductive Insertion Mediated by Organic Mixed-Valence in a Ferric Semiquinoid Metal-Organic Framework. *J. Am. Chem. Soc.* **2015**, *137*, 15703–15711.
- (19) Zhang, X.; Vermeulen, N. A.; Huang, Z.; Cui, Y.; Liu, J.; Krzyaniak, M. D.; Li, Z.; Noh, H.; Wasielewski, M. R.; Delferro, M.; Farha, O. K. Effect of Redox “Non-Innocent” Linker on the Catalytic Activity of Copper-Catecholate-Decorated Metal-Organic Frameworks. *ACS Appl. Mater. Interfaces* **2018**, *10*, 635–641.
- (20) Mendt, M.; Gutt, F.; Kavooosi, N.; Bon, V.; Senkovska, I.; Kaschel, S.; Pöppel, A. EPR Insights into Switchable and Rigid Derivatives of the Metal-Organic Framework DUT-8(Ni) by NO Adsorption. *J. Phys. Chem. C* **2016**, *120*, 14246–14259.
- (21) Okawa, H.; Sadakiyo, M.; Yamada, T.; Maesato, M.; Ohba, M.; Kitagawa, H. Proton-Conductive Magnetic Metal-Organic Frameworks, $\{\text{NR}_3(\text{CH}_2\text{COOH})\}[\text{M}_a^{\text{II}}\text{M}_b^{\text{III}}(\text{ox})_3]$: Effect of Carboxyl Residue upon Proton Conduction. *J. Am. Chem. Soc.* **2013**, *135*, 2256–2262.
- (22) Ren, J.; Ledwaba, M.; Musyoka, N. M.; Langmi, H. W.; Mathe, M.; Liao, S.; Pang, W. Structural Defects in Metal-Organic Frameworks (MOFs): Formation, Detection and Control towards Practices of Interests. *Coord. Chem. Rev.* **2017**, *349*, 169–197.
- (23) Wu, H.; Chua, Y. S.; Krungleviciute, V.; Tyagi, M.; Chen, P.; Yildirim, T.; Zhou, W. Unusual and Highly Tunable Missing-Linker Defects in Zirconium Metal-Organic Framework UiO-66 and Their Important Effects on Gas Adsorption. *J. Am. Chem. Soc.* **2013**, *135*, 10525–10532.
- (24) Sholl, D. S.; Lively, R. P. Defects in Metal–Organic Frameworks: Challenge or Opportunity? *J. Phys. Chem. Lett.* **2015**, *6*, 3437–3444.
- (25) Zhang, X. X.; Chui, S. S.-Y.; Williams, I. D. Cooperative Magnetic Behavior in the Coordination Polymers $[\text{Cu}_3(\text{TMA})_2\text{L}_3]$ (L = H_2O , pyridine). *J. Appl. Phys.* **2000**, *87*, 6007–6009.
- (26) Hicks, R. G. *Stable Radicals – Fundamentals and Applied Aspects of Odd-Electron Compounds*; Wiley, 2010.
- (27) Zwoliński, K. M.; Chmielewski, M. J. TEMPO-Appended Metal-Organic Frameworks as Highly Active, Selective, and Reusable Catalysts for Mild Aerobic Oxidation of Alcohols. *ACS Appl. Mater. Interfaces* **2017**, *9*, 33956–33967.
- (28) Zhuang, J.-L.; Liu, X.-Y.; Zhang, Y.; Wang, C.; Mao, H.-L.; Guo, J.; Du, X.; Zhu, S.-B.; Ren, B.; Terfort, A. Zr-Metal-Organic Frameworks Featuring TEMPO Radicals: Synergistic Effect between TEMPO and Hydrophilic Zr-Node Defects Boosting Aerobic Oxidation of Alcohols. *ACS Appl. Mater. Interfaces* **2019**, *11*, 3034–3043.
- (29) Maspoch, D.; Ruiz-Molina, D.; Veciana, J. Magnetic nanoporous coordination polymers. *J. Mater. Chem.* **2004**, *14*, 2713–2723.
- (30) Li, L.; Matsuda, R.; Tanaka, I.; Sato, H.; Kanoo, P.; Jeon, H. J.; Foo, M. L.; Wakamiya, A.; Murata, Y.; Kitagawa, S. A Crystalline Porous Coordination Polymer Decorated with Nitroxyl Radicals Catalyzes Aerobic Oxidation of Alcohols. *J. Am. Chem. Soc.* **2014**, *136*, 7543–7546.
- (31) Faust, T. B.; D’Alessandro, D. M. Radicals in Metal-Organic Frameworks. *RSC Adv.* **2014**, *4*, 17498–17512.
- (32) Blatter, H. M.; Lukaszewski, H. A New Stable Radical. *Tetrahedron Lett.* **1968**, *9*, 2701–2705.
- (33) Neugebauer, F. A.; Umminger, I. Über 1,4-Dihydro-1,2,4-benzotriazinyl-Radikale. *Chem. Ber.* **1980**, *113*, 1205–1225.
- (34) Constantinides, C. P.; Koutentis, P. A.; Loizou, G. Synthesis of 7-aryl/heteraryl-1,3-diphenyl-1,2,4-benzotriazinyls via Palladium Catalyzed Stille and Suzuki-Miyaura Reactions. *Org. Biomol. Chem.* **2011**, *9*, 3122–3125.
- (35) Bodzioch, A.; Zheng, M.; Kaszyński, P.; Utecht, G. Functional Group Transformations in Derivatives of 1,4-Dihydrobenzo[1,2,4]-triazinyl Radical. *J. Org. Chem.* **2014**, *79*, 7294–7310.
- (36) Morgan, I. S.; Peuronen, A.; Hänninen, M. M.; Reed, R. W.; Clérac, R.; Tuononen, H. M. 1-Phenyl-3-(pyrid-2-yl)benzo[e][1,2,4]-triazinyl: The First “Blatter Radical” for Coordination Chemistry. *Inorg. Chem.* **2014**, *53*, 33–35.
- (37) Morgan, I. S.; Mansikkamäki, A.; Zissimou, G. A.; Koutentis, P. A.; Rouzières, M.; Clérac, R.; Tuononen, H. M. Coordination Complexes of a Neutral 1,2,4-Benzotriazinyl Radical Ligand: Synthesis, Molecular and Electronic Structures, and Magnetic Properties. *Chem. - Eur. J.* **2015**, *21*, 15843–15853.
- (38) Liu, Y.; Li, J.-R.; Verdegaal, W. M.; Liu, T.-F.; Zhou, H.-C. Isostructural Metal-Organic Frameworks Assembled from Functionalized Diisophthalate Ligands through a Ligand-Truncation Strategy. *Chem. - Eur. J.* **2013**, *19*, 5637–5643.
- (39) Sheveleva, A. M.; Kolokolov, D. I.; Gabrienko, A. A.; Stepanov, A. G.; Gromilov, S. A.; Shundrina, I. K.; Sagdeev, R. Z.; Fedin, M. V.; Bagryanskaya, E. G. Structural Dynamics in “Breathing” Metal-Organic Framework Studied by Electron Paramagnetic Resonance of Nitroxide Spin Probes. *J. Phys. Chem. Lett.* **2014**, *5*, 20–24.
- (40) Nasalevich, M. A.; Becker, R.; Ramos-Fernandez, E. V.; Castellanos, S.; Veber, S. L.; Fedin, M. V.; Kapteijn, F.; Reek, J. N. H.; van der Vlugt, J. I.; Gascon, J. Co@NH₂-MIL-125(Ti): Cobaloxime-Derived Metal-Organic Framework-Based Composite for Light-Driven H₂ Production. *Energy Environ. Sci.* **2015**, *8*, 364–375.

- (41) Nasalevich, M. A.; Hendon, C. H.; Santaclara, J. G.; Svane, K.; van der Linden, B.; Veber, S. L.; Fedin, M. V.; Houtepen, A. J.; van der Veen, M. A.; Kapteijn, F.; Walsh, A.; Gascon, J. Electronic Origins of Photocatalytic Activity in d^0 Metal Organic Frameworks. *Sci. Rep.* **2016**, *6*, 23676.
- (42) Poryvaev, A. S.; Sheveleva, A. M.; Kolokolov, D. I.; Stepanov, A. G.; Bagryanskaya, E. G.; Fedin, M. V. Mobility and Reactivity of 4-Substituted TEMPO Derivatives in Metal-Organic Framework MIL-53(Al). *J. Phys. Chem. C* **2016**, *120*, 10698–10704.
- (43) Sheveleva, A. M.; Anikeenko, A. V.; Poryvaev, A. S.; Kuzmina, D. L.; Shundrina, I. K.; Kolokolov, D. I.; Stepanov, A. G.; Fedin, M. V. Probing Gas Adsorption in Metal-Organic Framework ZIF-8 by EPR of Embedded Nitroxides. *J. Phys. Chem. C* **2017**, *121*, 19880–19886.
- (44) Santaclara, J. G.; Olivos-Suarez, A. I.; Gonzalez-Nelson, A.; Osadchii, D.; Nasalevich, M. A.; van der Veen, M. A.; Kapteijn, F.; Sheveleva, A. M.; Veber, S. L.; Fedin, M. V.; Murray, A. T.; Hendon, C. H.; Walsh, A.; Gascon, J. Revisiting the Incorporation of Ti(IV) in UiO-type Metal-Organic Frameworks: Metal Exchange versus Grafting and Their Implications on Photocatalysis. *Chem. Mater.* **2017**, *29*, 8963–8967.
- (45) Poryvaev, A. S.; Sheveleva, A. M.; Demakov, P. A.; Arzumanov, S. S.; Stepanov, A. G.; Dybtsev, D. N.; Fedin, M. V. Pulse EPR Study of Gas Adsorption in Cu^{2+} -doped Metal-Organic Framework $[\text{Zn}_2(1,4\text{-bdc})_2(\text{dabco})]$. *Appl. Magn. Reson.* **2018**, *49*, 255–264.
- (46) Osadchii, D.; Olivos Suarez, A. I.; Szécényi, Á.; Li, G.; Nasalevich, M. A.; Dugulan, I.; Serra-Crespo, P.; Hensen, E. J. M.; Veber, S. L.; Fedin, M. V.; Sankar, G.; Pidko, E. A.; Gascon, J. Isolated Fe Sites in Metal Organic Framework Catalyze the Direct Conversion of Methane to Methanol. *ACS Catal.* **2018**, *8*, 5542–5548.
- (47) Iglesias-Juez, A.; Castellanos, S.; Monte, M.; Agostini, G.; Osadchii, D.; Nasalevich, M. A.; Santaclara, J. G.; Olivos Suarez, A. I.; Veber, S. L.; Fedin, M. V.; Gascón, J. Illuminating the Nature and Behavior of the Active Center: The Key for Photocatalytic H_2 Production in $\text{Co}@\text{NH}_2\text{-MIL-125(Ti)}$. *J. Mater. Chem. A* **2018**, *6*, 17318–17322.
- (48) Pöppl, A.; Kunz, S.; Himsl, D.; Hartmann, M. CW and Pulsed ESR Spectroscopy of Cupric Ions in the Metal-Organic Framework Compound $\text{Cu}_3(\text{BTC})_2$. *J. Phys. Chem. C* **2008**, *112*, 2678–2684.
- (49) Jee, B.; Koch, K.; Moschkowitz, L.; Himsl, D.; Hartman, M.; Pöppl, A. Electron Spin Resonance Study of Nitroxide Radical Adsorption at Cupric Ions in the Metal-Organic Framework Compound $\text{Cu}_3(\text{btc})_2$. *J. Phys. Chem. Lett.* **2011**, *2*, 357–361.
- (50) Jee, B.; St. Petkov, P.; Vayssilov, G. N.; Heine, T.; Hartmann, M.; Pöppl, A. A Combined Pulsed Electron Paramagnetic Resonance Spectroscopic and DFT Analysis of the $^{13}\text{CO}_2$ and ^{13}CO Adsorption on the Metal-Organic Framework $\text{Cu}_{2.97}\text{Zn}_{0.03}(\text{btc})_2$. *J. Phys. Chem. C* **2013**, *117*, 8231–8240.
- (51) Jee, B.; Hartmann, M.; Pöppl, A. H. D and HD Adsorption upon the Metal-Organic Framework $[\text{CuZn}(\text{btc})]$ Studied by Pulsed ENDOR and HYSCORE Spectroscopy. *Mol. Phys.* **2013**, *111*, 2950–2966.
- (52) Šimėnas, M.; Kobalz, M.; Mendt, M.; Eckold, P.; Krautscheid, H.; Banys, J.; Pöppl, A. Synthesis, Structure, and Electron Paramagnetic Resonance Study of a Mixed Valent Metal-Organic Framework Containing Cu_2 Paddle-Wheel Units. *J. Phys. Chem. C* **2015**, *119*, 4898–4907.
- (53) Friedländer, S.; Šimėnas, M.; Kobalz, M.; Eckold, P.; Ovchar, O.; Belous, A. G.; Banys, J.; Krautscheid, H.; Pöppl, A. Single Crystal Electron Paramagnetic Resonance with Dielectric Resonators of Mononuclear Cu^{2+} Ions in a Metal-Organic Framework Containing Cu_2 Paddle Wheel Units. *J. Phys. Chem. C* **2015**, *119*, 19171–19179.
- (54) Šimėnas, M.; Jee, B.; Hartmann, M.; Banys, J.; Pöppl, A. Adsorption and Desorption of HD on the Metal-Organic Framework $\text{Cu}_{2.97}\text{Zn}_{0.03}(\text{Btc})_2$ Studied by Three-Pulse ESEEM Spectroscopy. *J. Phys. Chem. C* **2015**, *119*, 28530–28535.
- (55) Šimėnas, M.; Matsuda, R.; Kitagawa, S.; Pöppl, A.; Banys, J. Electron Paramagnetic Resonance Study of Guest Molecule-Influenced Magnetism in Kagome Metal-Organic Framework. *J. Phys. Chem. C* **2016**, *120*, 27462–27467.
- (56) Friedländer, S.; Petkov, P. St.; Bolling, F.; Kultraeva, A.; Böhlmann, W.; Ovchar, O.; Belous, A. G.; Heine, T.; Pöppl, A. Continuous-Wave Single-Crystal Electron Paramagnetic Resonance of Adsorption of Gases to Cupric Ions in the Zn(II) -Doped Porous Coordination Polymer $\text{Cu}_{2.965}\text{Zn}_{0.035}(\text{btc})_2$. *J. Phys. Chem. C* **2016**, *120*, 27399–27411.
- (57) Xu, Z.-X.; Tan, Y.-X.; Fu, H.-R.; Liu, J.; Zhang, J. Homochiral Metal–Organic Frameworks with Enantiopure Proline Units for the Catalytic Synthesis of β -Lactams. *Inorg. Chem.* **2014**, *53*, 12199–12204.
- (58) Hofer, P.; Grupp, A.; Nebenfuhr, H.; Mehring, M. Hyperfine Sublevel Correlation (HYSCORE) Spectroscopy - a 2D Electron-Spin-Resonance Investigation of the Squaric Acid Radical. *Chem. Phys. Lett.* **1986**, *132*, 279–282.
- (59) Stoll, S.; Schweiger, A. EasySpin, a Comprehensive Software Package for Spectral Simulation and Analysis in EPR. *J. Magn. Reson.* **2006**, *178*, 42–55.
- (60) Constantinides, C. P.; Berezin, A. A.; Zissimou, G. A.; Manoli, M.; Leitun, G. M.; Bendikov, M.; Probert, M. R.; Rawson, J. M.; Koutentis, P. A. A Magnetostructural Investigation of an Abrupt Spin Transition for 1-Phenyl-3-trifluoromethyl-1,4-dihydrobenzo[e]-[1,2,4]triazin-4-yl. *J. Am. Chem. Soc.* **2014**, *136*, 11906–11909.
- (61) Xiong, X.; Jiang, Y.; Ma, D. Assembly of N,N -Disubstituted Hydrazines and 1-Aryl-1H-indazoles via Copper-Catalyzed Coupling Reactions. *Org. Lett.* **2012**, *14*, 2552.
- (62) Fomina, I.; Dobrokhotova, Z.; Aleksandrov, G.; Bogomyakov, A.; Fedin, M.; Dolganov, A.; Magdesieva, T.; Novotortsev, V.; Eremenko, I. Influence of the Nature of Organic Components in Dinuclear Copper(II) Pivalates on the Composition of Thermal Decomposition Products. *Polyhedron* **2010**, *29*, 1734–1746.
- (63) Bencini, A.; Gatteschi, D. *EPR of Exchange Coupled Systems*; Springer-Verlag: Berlin, 1990.
- (64) Jeschke, G.; Schweiger, A. *Principles of Pulse EPR*; Oxford University Press, 2001.
- (65) Liu, Y.; Her, J. H.; Dailly, A.; Ramirez-Cuesta, A. J.; Neumann, D. A.; Brown, C. M. Reversible Structural Transition in MIL-53 with Large Temperature Hysteresis. *J. Am. Chem. Soc.* **2008**, *130*, 11813–11818.
- (66) Mendt, M.; Jee, B.; Stock, N.; Ahnfeldt, T.; Hartmann, M.; Himsl, D.; Pöppl, A. Structural Phase Transitions and Thermal Hysteresis in the Metal-Organic Framework Compound MIL-53 as Studied by Electron Spin Resonance Spectroscopy. *J. Phys. Chem. C* **2010**, *114*, 19443–19451.
- (67) Loiseau, T.; Serre, C.; Huguenard, C.; Fink, G.; Taulelle, F.; Henry, M.; Bataille, T.; Ferey, G. A Rationale for the Large Breathing of the Porous Aluminum Terephthalate (MIL-53) Upon Hydration. *Chem. - Eur. J.* **2004**, *10*, 1373–1382.
- (68) Krause, S.; Bon, V.; Senkovska, I.; Stoeck, U.; Wallacher, D.; Tobbens, D. M.; Zander, S.; Pillai, R. S.; Maurin, G.; Coudert, F. X.; Kaskel, S. A Pressure-Amplifying Framework Material with Negative Gas Adsorption Transitions. *Nature* **2016**, *532*, 348–352.
- (69) Krause, S.; Bon, V.; Senkovska, I.; Tobbens, D. M.; Wallacher, D.; Pillai, R. S.; Maurin, G.; Kaskel, S. The Effect of Crystallite Size on Pressure Amplification in Switchable Porous Solids. *Nat. Commun.* **2018**, *9*, 1573.
- (70) Murnaghan, K. D.; Carbonera, C.; Toupet, L.; Griffin, M.; Dirtu, M. M.; Desplanches, C.; Garcia, Y.; Collet, E.; Letard, J.-F.; Morgan, G. G. Spin-State Ordering on One Sub-lattice of a Mononuclear Iron(III) Spin Crossover Complex Exhibiting LIESST and TIESST. *Chem. - Eur. J.* **2014**, *20*, 5613–5618.
- (71) Gómez, V.; Sáenz de Pipaón, C.; Maldonado-Illescas, P.; Waerenborgh, J. C.; Martin, E.; Benet-Buchholz, J.; Galán-Mascarós, J. R. Easy Excited-State Trapping and Record High TTIEST in a Spin-Crossover Polyanionic FeII Trimer. *J. Am. Chem. Soc.* **2015**, *137*, 11924–11927.
- (72) Fu, Y.; Kang, Z.; Yin, J.; Cao, W.; Tu, Y.; Wang, Q.; Kong, X. Duet of Acetate and Water at the Defects of Metal-Organic Frameworks. *Nano Lett.* **2019**, *19*, 1618.